Studies of granularity of a hadronic calorimeter for tens-of-TeV jets at a 100 TeV pp collider

C.-H. Yeh[a], S.V. Chekanov[b], A.V. Kotwal[c], J. Proudfoot[b], S. Sen[c], N.V. Tran[d], S.-S. Yu[a]

[a] *Department of Physics, National Central University, Chung-Li, Taoyuan City 32001, Taiwan*
[b] *HEP Division, Argonne National Laboratory, 9700 S. Cass Avenue, Argonne, IL 60439, USA.*
[c] *Department of Physics, Duke University, USA*
[d] *Fermi National Accelerator Laboratory*
[e] *Department of Physics, Michigan State University, 220 Trowbridge Road, East Lansing, MI 48824*

Abstract

Jet substructure variables for hadronic jets with transverse momenta in the range from 2.5 TeV to 20 TeV were studied using several designs for the spatial size of calorimeter cells. The studies used the full Geant4 simulation of calorimeter response combined with realistic reconstruction of calorimeter clusters. In most cases, the results indicate that the performance of jet-substructure reconstruction improves with reducing cell size of a hadronic calorimeter from $\Delta\eta \times \Delta\phi = 0.087 \times 0.087$ to 0.022×0.022.

Keywords: multi-TeV physics, pp collider, future hadron colliders, FCC, SppC

1. Introduction

Particle collisions at energies beyond those attained at the LHC will lead to many challenges for detector technologies. Future circular pp colliders such as the European initiatives, high-energy LHC (HE-LHC) and FCC-hh [1] and the Chinese initiative, SppC [2] will measure high-momentum bosons (W, Z, H) and top quarks with highly-collimated decay products that form jets. Jet substructure techniques are used to identify such boosted particles, and thus can maximize the physics potential of the future colliders.

The reconstruction of jet substructure variables for collimated jets with transverse momenta above 10 TeV requires an appropriate detector design. The most important detector systems for reconstruction of such jets are tracking and calorimetry. Recently, a number of studies [3, 4, 5] have been discussed using various fast simulation tools, such as Delphes [6], in which momenta of particles are smeared to mimic detector response.

A major step towards the usage of full Geant4 simulation to verify the granularity requirements for calorimeters was made in [7]. These studies have illustrated a significant impact of granularity of electromagnetic (ECAL) and hadronic (HCAL) calorimeters

Email addresses: `jwzuzelski18@gmail.com` (C.-H. Yeh), `chekanov@anl.gov` (S.V. Chekanov), `ashutosh.kotwal@duke.edu` (A.V. Kotwal), `proudfoot@anl.gov` (J. Proudfoot), `sourav.sen@duke.edu` (S. Sen), `ntran@fnal.gov` (N.V. Tran), `syu@cern.ch` (S.-S. Yu)

on the cluster separation between two particles. It was concluded that high granularity is essential in resolving two close-by particles for energies above 100 GeV.

This paper takes the next step in understanding this problem in terms of high-level quantities typically used in physics analyses. Similar to the studies presented in [7], this paper is based on a full Geant4 simulation with realistic jet reconstruction.

2. Simulation of detector response

The description of the detector and software used for this study is discussed in [7]. We use the SiFCC detector geometry with a software package that provides a versatile environment for simulations of detector performance, testing new technology options, and event reconstruction techniques for future 100 TeV colliders.

The baseline detector discussed in [7] uses a steel-scintillator hadronic calorimeter with a transverse cell size of 5×5 cm^2, which corresponds to $\Delta\eta \times \Delta\phi = 0.022 \times 0.022$, where η is the pseudorapidity, $\eta \equiv -\ln\tan(\theta/2)$, and ϕ is the azimuthal angle. The depth of the HCAL in the barrel region is 11.25 interaction lengths (λ_I). The HCAL has 64 longitudinal layers in the barrel and the endcap regions.

In addition to the baseline HCAL geometry, several geometry variations were considered. We used the HCAL with transverse cell size of 20×20 cm^2, 2×2 cm^2 and 1×1 cm^2. In the terms of $\Delta\eta \times \Delta\phi$, such cell sizes correspond to 0.087×0.087, 0.0087×0.0087 and 0.0043×0.0043, respectively.

The GEANT4 (version 10.3) [8] simulation of calorimeter response was followed by the full reconstruction of calorimeter clusters formed by the Pandora algorithm [9, 10]. Calorimeter clusters were built from calorimeter hits in the ECAL and HCAL after applying the corresponding sampling fractions. No other corrections are applied. Hadronic jets were reconstructed with the FastJet package [11] using the anti-k_T algorithm [12] with a distance parameter of 0.5.

In the following discussion, we use the simulations of a heavy Z' boson, a hypothetical gauge boson that arises from extensions of the electroweak symmetry of the Standard Model. The Z' bosons were simulated with the masses M = 5, 10, 20 and 40 TeV. The lowest value represents a typical mass that is within the reach of the LHC experiments. The resonance mass of 40 TeV represents the physics reach for a 100 TeV collider. The Z' bosons are forced to decay to two light-flavor quark ($q\bar{q}$), W^+W^- or $t\bar{t}$ final states, where the W bosons and t quarks decay hadronically. In these scenarios, two highly-boosted jets are produced, which are typically back-to-back in the laboratory frame. The typical transverse momenta of the jets are $\simeq M/2$. The main difference between the considered decay modes lies in the different jet substructures. In the case of the $q\bar{q}$ decays, jets do not have any internal structure. In the case of the W^+W^- final state, each jet has two subjets because of the decay $W \to q\bar{q}$. In the case of hadronic top decays, jets have three subjets due to the decay $t \to W^+ b \to q\bar{q}b$. The signal events were generated using the Pythia8 generator with the default settings, ignoring interference with SM processes. The event samples used in this paper are available from the HepSim database [13].

3. Studies of jet properties

We consider several variables that characterize jet substructure using different calorimeter granularities. The question we want to answer is, how closely the reconstructed jet substructure variables reflect the input "truth" values that are reconstructed using particles directly from the PYTHIA8 generator.

In this study we use the jet effective radius and jet splitting scales as benchmark variables to study jet substructure properties. The effective radius is the average of the energy-weighted radial distance δR_i in $\eta - \phi$ space of jet constituents. It is defined as $(1/E)\sum_i e_i \delta R_i$, where E is the energy of the jet and e_i is the energy of a calorimeter constituent cluster i at the distance δR_i from the jet center. The sum runs over all constituents of the jet. This variable has been studied for multi-TeV jets in Ref. [14]. A jet k_T splitting scale [15] is defined as a distance measure used to form jets by the k_T recombination algorithm [16, 17]. This variable has been studied by ATLAS [18], and more recently in the context of 100 TeV physics [14]. The splitting scale is defined as $\sqrt{d_{12}} = \min(p_T^1, p_T^2) \times \delta R_{12}$ [18] at the final stage of the k_T clustering, where two subjets are merged into the final jet.

Figures 1 and 2 show the distributions of the jet effective radius and jet splitting scale for different jet transverse momenta and HCAL granularities. The reconstructed-level distributions disagree significantly with the distributions reconstructed using truth-level particles. The distributions reconstructed with cell size 1×1 cm^2 are closest to the truth-level variables. The distributions reconstructed using the cell size of 20×20 cm^2, show the largest discrepancy with the truth-level variables. Note that, in terms of similarity of reconstructed distributions to the truth-level distributions, there is no significant difference between 5×5 cm^2, 2×2 cm^2 and 1×1 cm^2 cell sizes.

This study confirms the baseline SiFCC detector geometry [7] that uses 5×5 cm^2 HCAL cells, corresponding to $\Delta\eta \times \Delta\phi = 0.022 \times 0.022$. Similar HCAL cell sizes, 0.025×0.025, were recently adopted for the baseline FCC-hh detector [19, 20] planned at CERN. Before the publication [7], such a choice for the HCAL cells was motivated by the studies of jet substructure using a fast detector simulation of boosted jets. In addition to the improvements in physics performance, the smaller HCAL cells reduce the required dynamic range for signal reconstruction [4], and thus can simplify the calorimeter readout.

It should be noted that the ATLAS and CMS detectors use the HCAL cell sizes in the barrel region which are close to $\Delta\eta \times \Delta\phi = 0.087 \times 0.087$. According to this study, such HCAL cell sizes are not optimal in terms of performance for tens-of-TeV jets.

In the following sections we consider several other physics-motivated variables that can shed light on the performance of the HCAL for tens-of-TeV jets.

4. Detector performance with soft drop mass

In this section, we use the jet mass computed with a specific algorithm, soft drop declustering, to study the performance with various detector cell sizes and resonance masses.

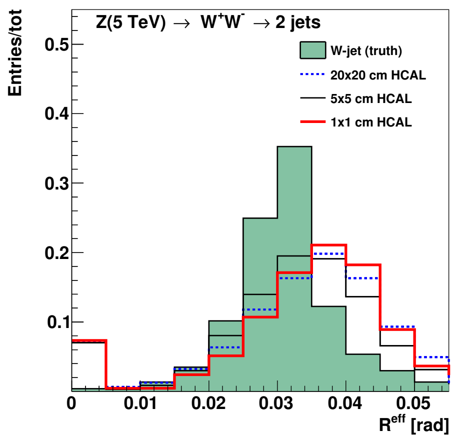

(a) 5 TeV

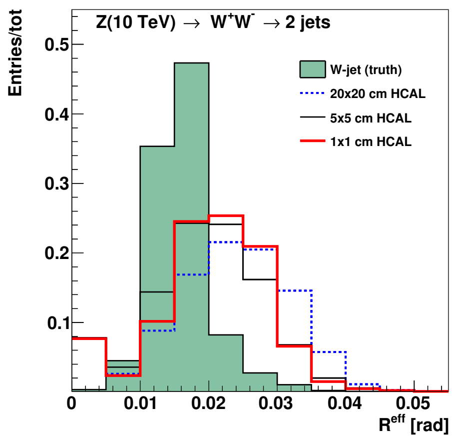

(b) 10 TeV

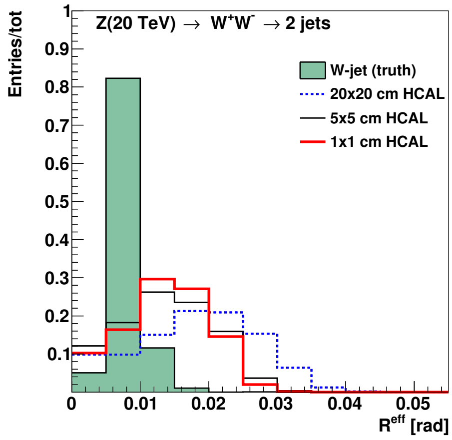

(c) 20 TeV

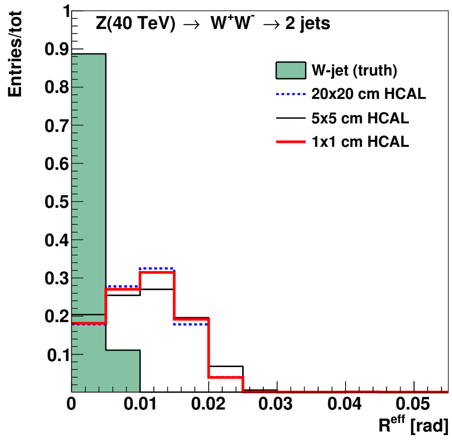

(d) 40 TeV

Figure 1: Jet effective radius for different jet transverse momenta and HCAL granularities.

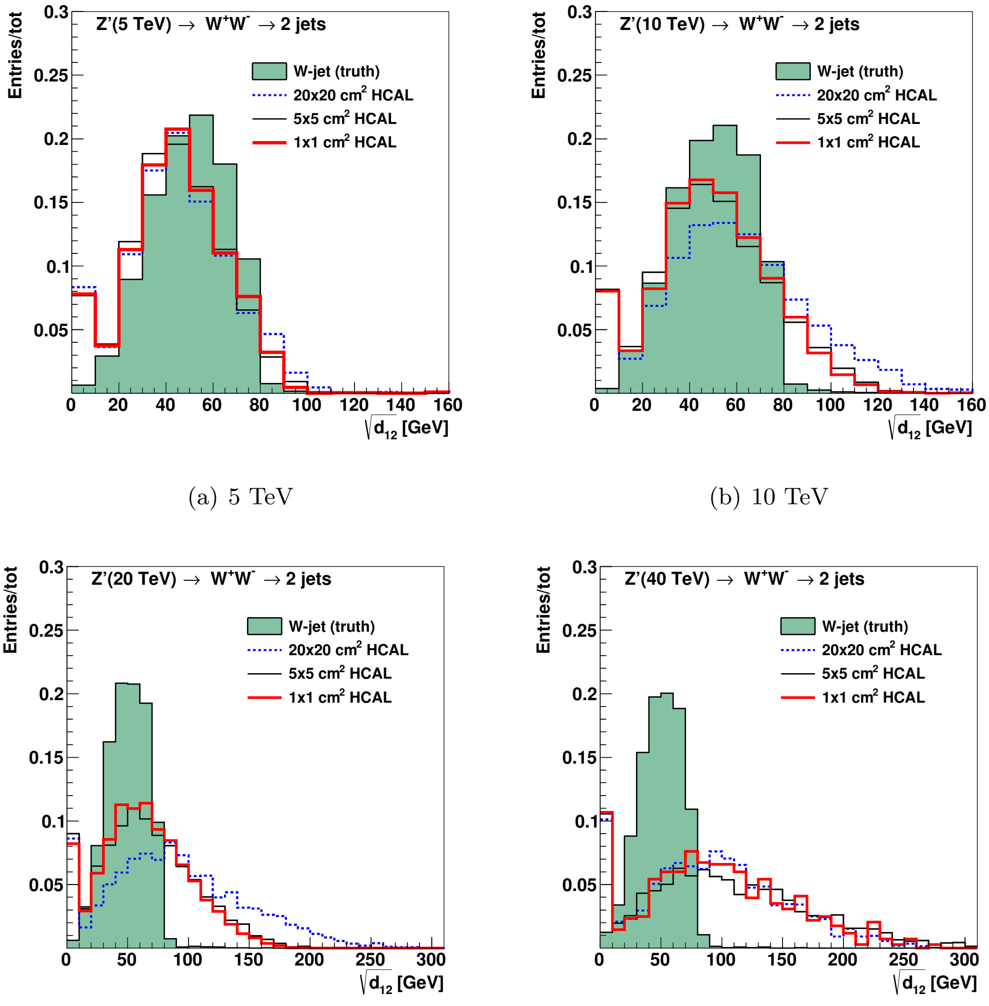

(a) 5 TeV

(b) 10 TeV

(c) 20 TeV

(d) 40 TeV

Figure 2: Jet splitting scale for different jet transverse momenta and HCAL granularity.

4.1. The technique of soft drop declustering

The soft drop declustering [21] is a grooming method that removes soft wide-angle radiation from a jet. The constituents of a jet j_0 are first reclustered using the Cambridge-Aachen (C/A) algorithm [22, 23]. Then, the jet j_0 is broken into two subjets j_1 and j_2 by undoing the last stage of C/A clustering. If the subjets pass the following soft drop condition, jet j_0 is the final soft-drop jet. Otherwise, the algorithm redefines j_0 to be the subjet with larger p_T (among j_1 and j_2) and iterates the procedure. The condition is,

$$\frac{\min(p_{T1}, p_{T2})}{p_{T1} + p_{T2}} > z_{\mathrm{cut}}(\frac{\Delta R_{12}}{R_0})^{\beta}, \tag{1}$$

where p_{T1} and p_{T2} are the transverse momenta of the two subjets, z_{cut} is soft drop threshold, ΔR_{12} is the distance between the two subjets in the rapidity-azimuthal plane (y-ϕ), R_0 is the characteristic radius of the original jet, and β is the angular exponent.

In our study, we compare the HCAL performance for the soft drop mass with $\beta = 0$ and $\beta = 2$. For $\beta = 0$, the soft drop condition depends only on the z_{cut}. For $\beta = 2$, the condition depends on the angular distance between the two subjets and z_{cut} and the algorithm becomes infrared and collinear safe.

4.2. Analysis method

We employ the following method to quantify the detector performance and determine the cell size that gives the best separation between signal and background. For each configuration of detector and resonance mass, we draw the receiver operating characteristic (ROC) curves in which the x-axis is the signal efficiency (ϵ_{sig}) and y-axis is the inverse of the background efficiency ($1/\epsilon_{\mathrm{bkg}}$). In order to scan the efficiencies of soft drop mass cuts, we vary the mass window as follows. We center the initial window on the median of the signal histogram, and increase its width symmetrically left and right in bins of 5 GeV. If one side of the mass window reaches the boundary of the mass histogram, we increase the width on the other side. For each mass window, the corresponding efficiencies ϵ_{sig} and ϵ_{bkg} give a point on the ROC curve.

4.3. Results and conclusion

Figures 3, 5, 7 and 9 show the distributions for the soft drop mass for $\beta = 0$ and $\beta = 2$ with different resonance masses and detector cell sizes; the signals considered are the $Z' \to WW$ and $Z' \to t\bar{t}$ processes. Figures 4, 6, 8 and 10 show the corresponding ROC curves for different detector cell sizes and resonance masses.

These studies show that the reconstruction of soft drop mass improves with decreasing HCAL cell sizes. Figures 4 and 6 show that for $\beta = 0$ the smallest detector cell size, 1×1 cm^2, has the best separation power at resonance masses of 5, 10, and 20 TeV when the signal is the $Z' \to WW$ process, and at resonance masses of 10 and 20 TeV when the signal is the $Z' \to t\bar{t}$ process. On the contrary, Figs. 8 and 10 show that for $\beta = 2$ the smallest detector cell size does not have improvements in the separation power when compared with larger cell sizes. In fact, the performance for the three cell sizes is similar. In addition, sometimes bigger cell sizes, 5×5 cm^2 or even 20×20 cm^2 have the best separation power.

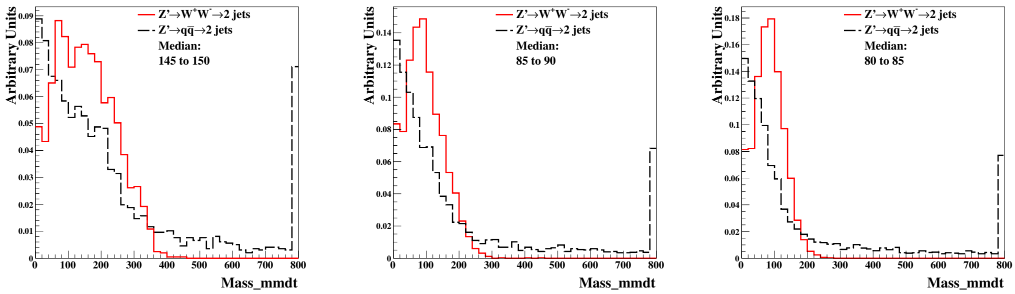

(a) 20×20 (cm^2) (b) 5×5 (cm^2) (c) 1×1 (cm^2)

Figure 3: Distributions of soft drop mass for β=0, with $M(Z') = 20$ TeV and three different detector cell sizes: 20×20, 5×5 and 1×1 cm^2. The signal (background) process is $Z' \to WW$ ($Z' \to q\bar{q}$).

Note that the separation between ROC curves depends on the physics variable and on the boost of the top quarks or the W bosons. For example, the similarity between the ROC curves shown in Fig. 6(a) is due to the insufficient boost of the top quarks. On the other hand, Fig. 6(d) does not show a difference between the ROC curves because the boost is too high.

We also find that the soft drop mass with $\beta = 0$ has better performance for distinguishing signal from background than with $\beta = 2$. Therefore, we will apply requirements on the soft drop mass with $\beta = 0$ when studying the other jet substructure variables.

5. Detector performance with jet substructure variables

In this section, we use several jet substructure variables to study the performance with various detector cell sizes and resonance masses.

5.1. *N-subjettiness*

The variable N-subjettiness [24], denoted by τ_N, is designed to “count” the number of subjet(s) in a large radius jet in order to separate signal jets from decays of heavy bosons and background jets from QCD processes. τ_N is the p_{T}-weighted angular distance between each jet constituent and the closest subjet axis:

$$\tau_N = \frac{1}{d_0}\sum_k p_{T,k}\,\mathrm{min}\{\Delta R_{1,k}, \Delta R_{2,k}, ...\Delta R_{N,k}\}, \tag{2}$$

with a normalization factor d_0:

$$d_0 = \sum_k p_{T,k} R_0.$$

The k index runs over all constituent particles in a given large radius jet, $p_{T,k}$ is the transverse momentum of each individual constituent, $\Delta R_{j,k} = \sqrt{(\Delta y)^2 + (\Delta\phi)^2}$ is the

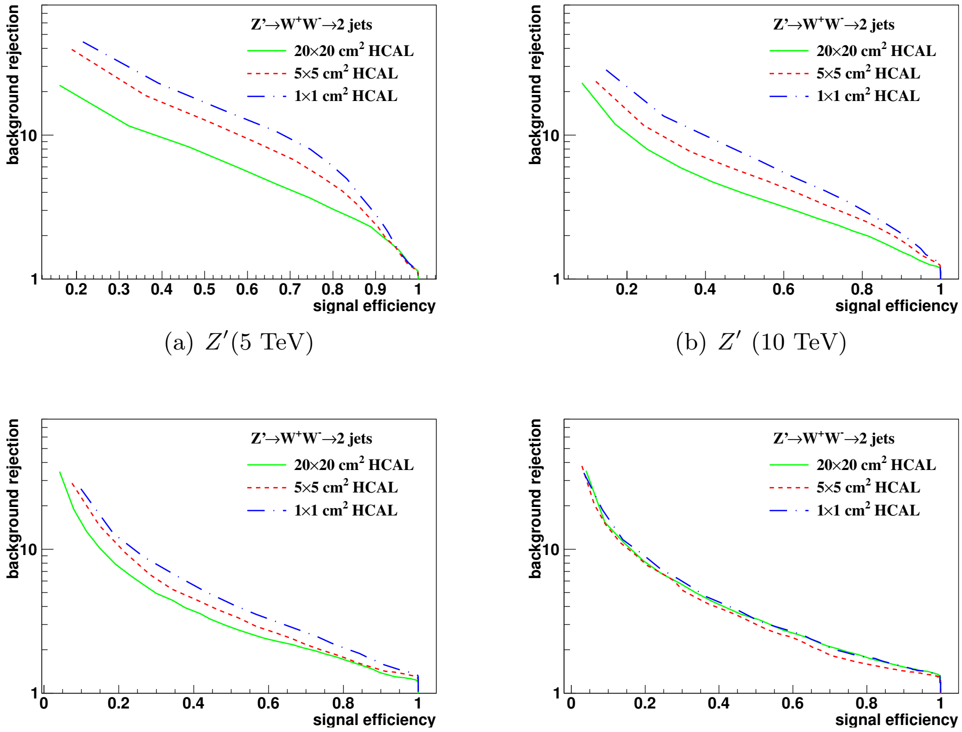

(a) Z'(5 TeV)

(b) Z' (10 TeV)

(c) Z' (20 TeV)

(d) Z' (40 TeV)

Figure 4: The ROC curves of soft drop mass selection for β=0 with resonance masses of 5, 10, 20 and 40 TeV. Three different detector cell sizes are compared: 20 $\times$ 20, 5 $\times$ 5, and 1 $\times$ 1 cm^2. The signal (background) process is $Z' \to WW$ ($Z' \to q\bar{q}$).

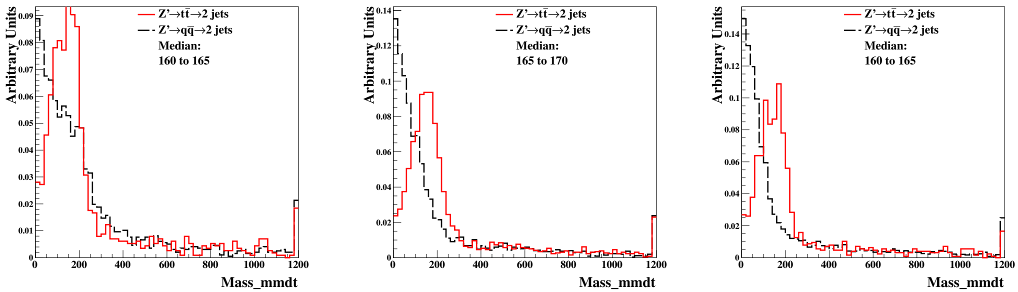

(a) 5 $\times$ 5 (cm^2)

(b) 20 $\times$ 20 (cm^2)

(c) 1 $\times$ 1 (cm^2)

Figure 5: Distributions of soft drop mass for β=0, with $M(Z')$ = 20 TeV and three different detector cell sizes: 20 $\times$ 20, 5 $\times$ 5, and 1 $\times$ 1 cm^2. The signal (background) process is $Z' \to t\bar{t}$ ($Z' \to q\bar{q}$).

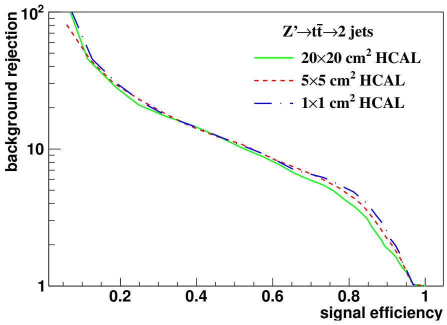

(a) Z' (5 TeV)

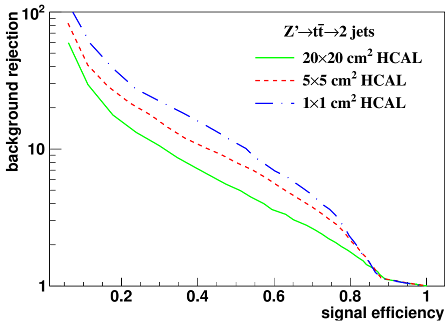

(b) Z' (10 TeV)

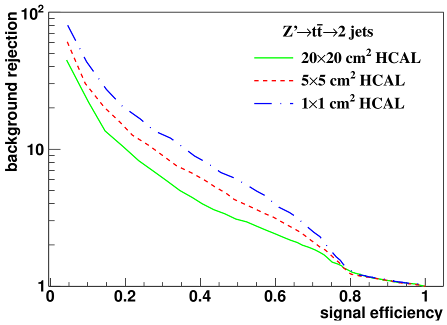

(c) Z' (20 TeV)

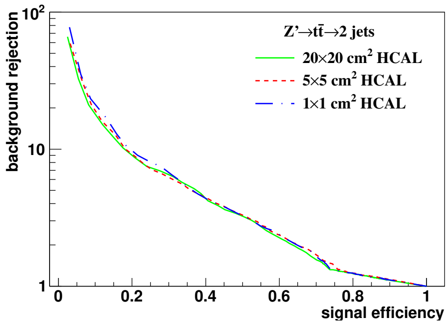

(d) Z' (40 TeV)

Figure 6: The ROC curves of soft drop mass selection for β=0 with resonance masses of 5, 10, 20 and 40 TeV. Three different detector cell sizes are compared: 20 × 20, 5 × 5, and 1 × 1 cm^2. The signal (background) process is $Z' \to t\bar{t}$ ($Z' \to q\bar{q}$).

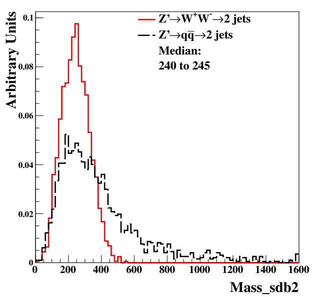

(a) 20 × 20 (cm^2)

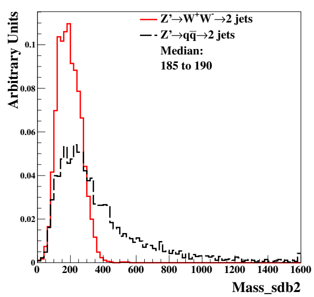

(b) 5 × 5 (cm^2)

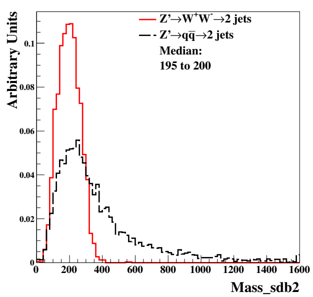

(c) 1 × 1 (cm^2)

Figure 7: Distributions of soft drop mass for $\beta = 2$, with $M(Z') = 20$ TeV and three different detector cell sizes: 20 × 20, 5 × 5 and 1 × 1 cm^2. The signal (background) process is $Z' \to WW$ ($Z' \to q\bar{q}$).

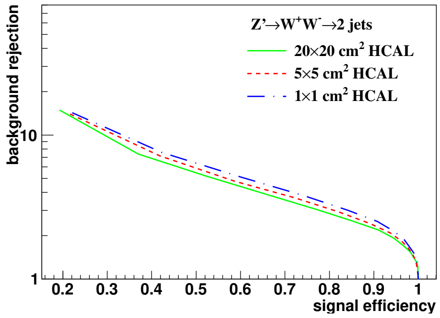

(a) Z' (5 TeV)

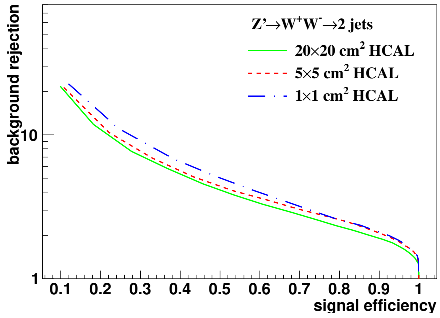

(b) Z' (10 TeV)

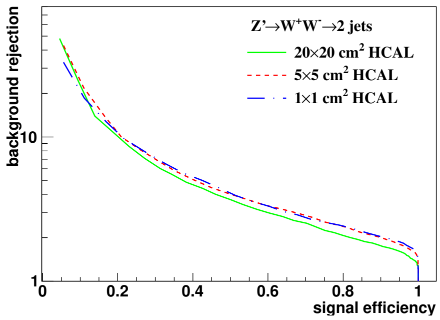

(c) Z' (20 TeV)

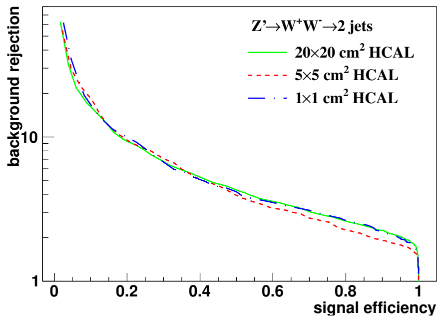

(d) Z' (40 TeV)

Figure 8: The ROC curves of soft drop mass selection for $\beta = 2$ with resonance masses of 5, 10, 20 and 40 TeV. Three different detector cell sizes are compared: 20×20, 5×5, and 1×1 cm^2. The signal (background) process is $Z' \to WW$ ($Z' \to q\bar{q}$).

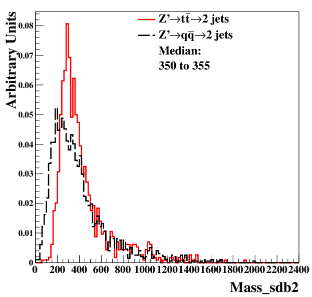

(a) 20×20 (cm^2)

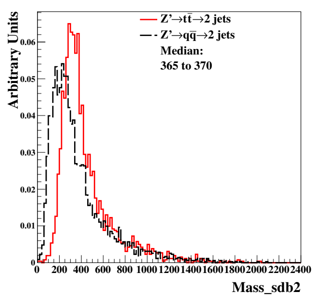

(b) 5×5 (cm^2)

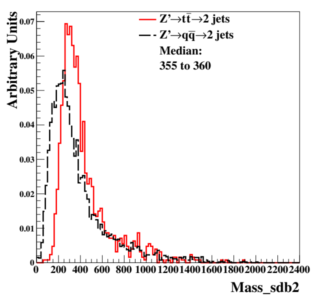

(c) 1×1 (cm^2)

Figure 9: Distributions of soft drop mass for $\beta = 2$, with $M(Z') = 20$ TeV and three different detector cell sizes: 20×20, 5×5, and 1×1 cm^2. The signal (background) process is $Z' \to t\bar{t}$ ($Z' \to q\bar{q}$).

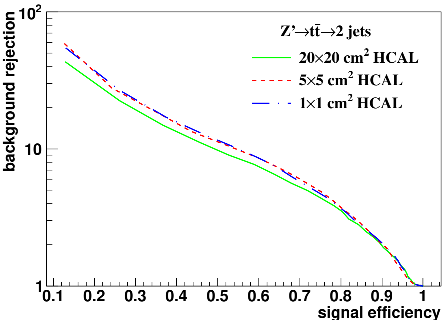

(a) Z'(5 TeV)

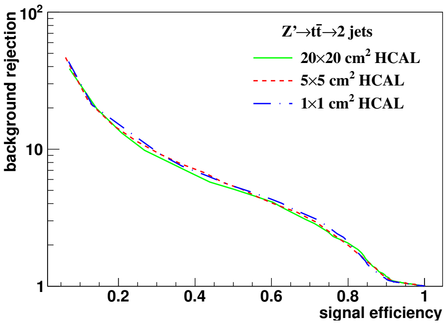

(b) Z'(10 TeV)

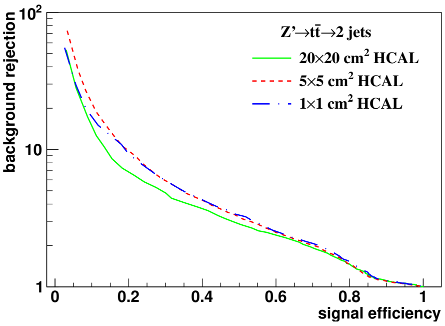

(c) Z'(20 TeV)

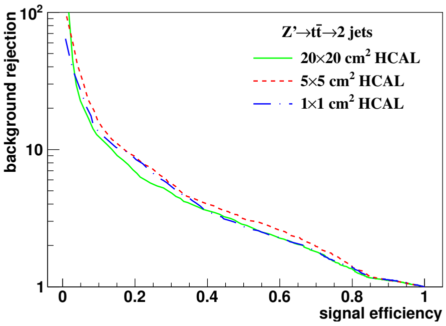

(d) Z'(40 TeV)

Figure 10: The ROC curves of soft drop mass selection for $\beta = 2$ with resonance masses of 5, 10, 20 and 40 TeV. Three different detector cell sizes are compared: 20×20, 5×5 and 1×1 cm^2. The signal (background) process is $Z' \to t\bar{t}$ ($Z' \to q\bar{q}$).

distance between the constituent k and the candidate subjet axis j in the $y - \phi$ plane. R_0 is the characteristic jet radius used in the anti-k_t jet algorithm.

This analysis uses the jet reconstruction described in Sect. 2. The subjet axes are obtained by running the exclusive k_t algorithm [25] and reversing the last N clustering steps. Namely, when τ_N is computed, the k_t algorithm is forced to return exactly N jets. If a large radius jet has N subjet(s), its τ_N is smaller than τ_{N-1}. Therefore, in our analysis, the ratios $\tau_{21} \equiv \tau_2/\tau_1$ and $\tau_{32} \equiv \tau_3/\tau_2$ are used to distinguish the one-prong background jets and the two-prong jets from W boson decays or the three-prong jets from top quark decays.

We use the ROC curves described in Sect. 4.2 to analyze the detector performance and determine the cell size that gives the best separation between signal and background processes. Following the suggestion of Ref. [26], the requirement on the soft drop mass with $\beta = 0$ is applied before the study of N-subjettiness. For each detector configuration and resonance mass, the soft drop mass prerequisite window is determined as follows. The window is initialized by the median bin of the soft drop mass histogram from simulated signal events as described in Sect. 4.2. Comparing the adjacent bins, the bin with the larger number of events is included to extend the mass window iteratively. The procedure is repeated until the prerequisite mass window cut reaches a signal efficiency of 75%.

With this *a-priori* mass window pre-selection, the signal and background efficiencies of various τ_{21} and τ_{32} window cuts are scanned. Since some of the background distributions have long tails and leak into the signal-dominated region, we use the following method based on the Neyman-Pearson lemma to determine the τ windows. First, we take the ratio of the signal to background τ_{21} (or τ_{32}) histograms. The window is initialized by the bin with the maximum signal to background ratio (S/N). Comparing the adjacent bins, the bin with the larger S/N is included to extend the τ_{21} (or τ_{32}) selection window. Every window has its corresponding ϵ_{sig} and $1/\epsilon_{\text{bkg}}$ and an ROC curve is mapped out.

In addition to the ROC curves, we use the so-called "Mann-Whitney" test [27] to quantify the detector performance. The value of the Mann-Whitney U variable is related to the area under the ROC curve; if the U value is bigger, it indicates the signal and background distributions have similar shapes and cannot be well-separated from each other. Vice versa, if the U value is smaller, we can achieve better signal and background separation.

Figures 11 and 13 show the distributions of τ_{21} and τ_{32} for $M(Z') = 20$ TeV after applying the requirement on the soft drop mass. The signals considered are the $Z' \to WW$ (for τ_{21}) and $Z' \to t\bar{t}$ (for τ_{32}) processes. Figures 12 and 14 present the ROC curves from different detector cell sizes and resonance masses, respectively. The smallest detector cell size (1×1 cm^2) does not have the best separation power. In fact, in some cases, the best separation power comes from a detector with bigger cell sizes (5×5 cm^2 and 20×20 cm^2).

Figure 17 presents the summary plots of τ_{21} and τ_{32} with various detector cell sizes and resonance masses using the Mann-Whitney test. For τ_{21} at smaller resonance masses, the detector performance improves when cell size is reduced. However, when the resonance mass increases, no improvement is observed using the smallest detector cell size (1×1 cm^2). The case for τ_{32} is similar to τ_{21}. It is interesting to note that at very large resonance masses, the large detector cell sizes (5×5 cm^2 and 20×20 cm^2) have a better separation power than the smallest cell size considered in this analysis.

5.2. Energy correlation function

The energy correlation function (ECF) [28] is defined as follows:

$$ECF(N,\beta) = \sum_{i_1<i_2<....<i_N \in J} \left(\prod_{a=1}^{N} p_{\mathrm{T}ia}\right) \left(\prod_{b=1}^{N-1} \prod_{c=b+1}^{N} R_{i_b i_c}\right)^{\beta}, \tag{3}$$

where the sum is over all constituents in jet J, p_{T} is the transverse momentum of each constituent, and R_{mn} is the distance between two constituents m and n in the y-ϕ plane. In order to use a dimensionless variable, a parameter r_N is defined:

$$r_N^{(\beta)} \equiv \frac{ECF(N+1,\beta)}{ECF(N,\beta)}. \tag{4}$$

The idea of r_N comes from N-subjettiness τ_N. Both r_N and τ_N are linear in the energy of the soft radiation for a system of N partons accompanied by soft radiation. In general, if the system has N subjets, $ECF(N+1,\beta)$ should be significantly smaller than $ECF(N,\beta)$. Therefore, we can use this feature to distinguish jets with different numbers of subjets. As in Sect. 5.1, the ratio r_N/r_{N-1}, denoted by C_N, (double-ratios of ECFs) is used to study the detector performance:

$$C_N^{(\beta)} \equiv \frac{r_N^{(\beta)}}{r_{N-1}^{(\beta)}} = \frac{ECF(N-1,\beta)ECF(N+1,\beta)}{ECF(N,\beta)^2}. \tag{5}$$

In our analysis, we set $N = 2$ and $\beta = 1$ (C_2^1).

Figure 15 presents the histograms of C_2^1 with $M(Z') = 20$ TeV after making the requirement on the soft drop mass. The signal considered is the $Z' \to WW$ process. Figure 16 shows the ROC curves from different detector cell sizes for each resonance mass. One can see that the smallest detector cell size (1×1 cm^2) does not have the best signal-to-background separation power. Figure 17 summarizes the result of the Mann-Whitney test for C_2^1. When the resonance mass increases, no improvement is observed with the smallest cell size.

6. Conclusions

The studies presented in this paper show that the reconstruction of jet substructure variables for future particle colliders will benefit from small cell sizes of the hadronic calorimeters. This conclusion was obtained using the realistic GEANT4 simulation of calorimeter response combined with reconstruction of calorimeter clusters used as inputs for jet reconstruction. Hadronic calorimeters that use the cell sizes of 20×20 cm^2 ($\Delta\eta \times \Delta\phi = 0.087 \times 0.087$) are least performant for almost every substructure variable considered in this analysis, for jet transverse momenta between 2.5 and 10 TeV. Such cell sizes are similar to those used for the ATLAS and CMS detectors at the LHC. In terms of reconstruction of physics-motivated quantities used for jet substructure studies, the performance of a hadronic callorimeter with $\Delta\eta \times \Delta\phi = 0.022 \times 0.022$ is, in

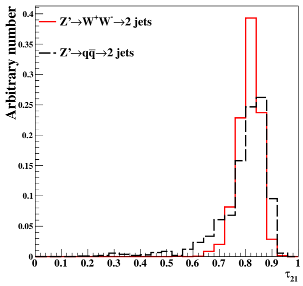

(a) 20×20 (cm^2)

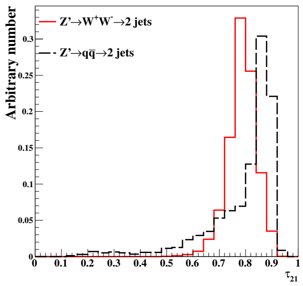

(b) 5×5 (cm^2)

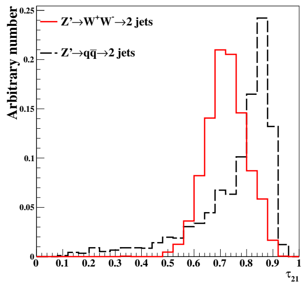

(c) 1×1 (cm^2)

Figure 11: Distributions of τ_{21} for $M(Z') = 20$ TeV for different detector granularities. Cell sizes of 20×20, 5×5, and 1×1 cm^2 are shown here.

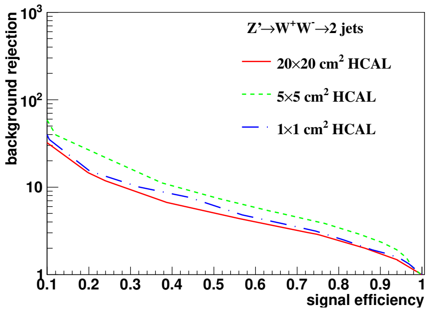

(a) Z'(5 TeV)

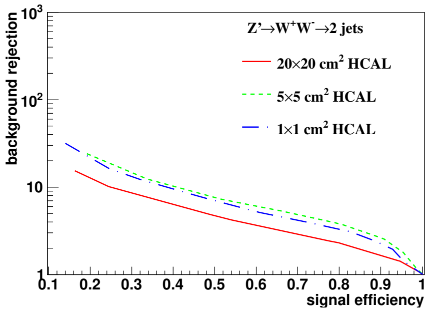

(b) Z'(10 TeV)

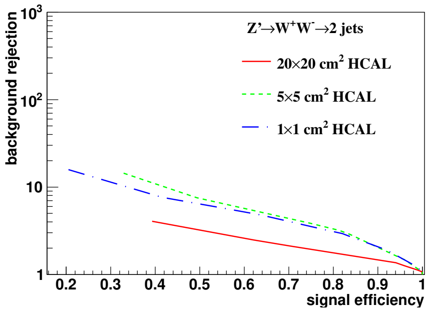

(c) Z'(20 TeV)

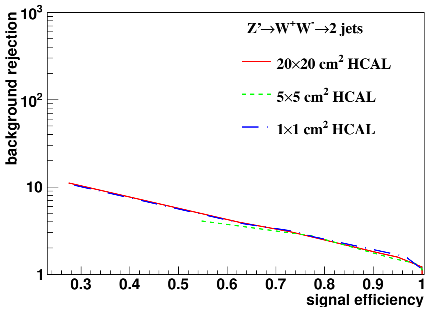

(d) Z'(40 TeV)

Figure 12: Signal efficiency versus background rejection rate using τ_{21}. Resonance masses of (a) 5 TeV, (b) 10 TeV, (c) 20 TeV and (d) 40 TeV are shown here. In each figure, the three ROC curves correspond to different cell sizes.

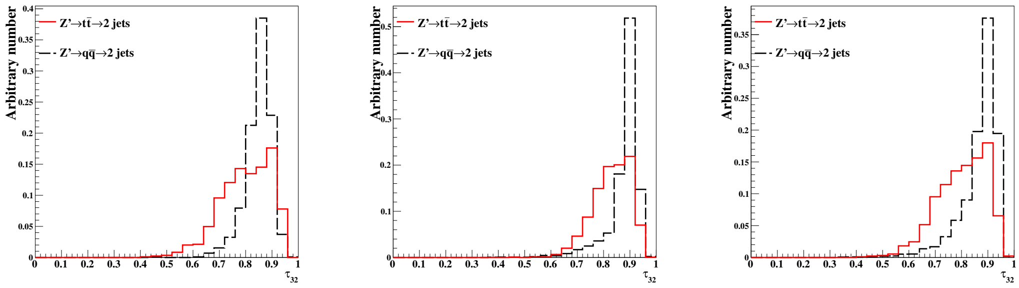

(a) 20×20 (cm^2) (b) 5×5 (cm^2) (c) 1×1 (cm^2)

Figure 13: Distributions of τ_{32} for $M(Z') = 20$ TeV for different detector granularities. Cell sizes of 20×20, 5×5, and 1×1 cm^2 are shown here.

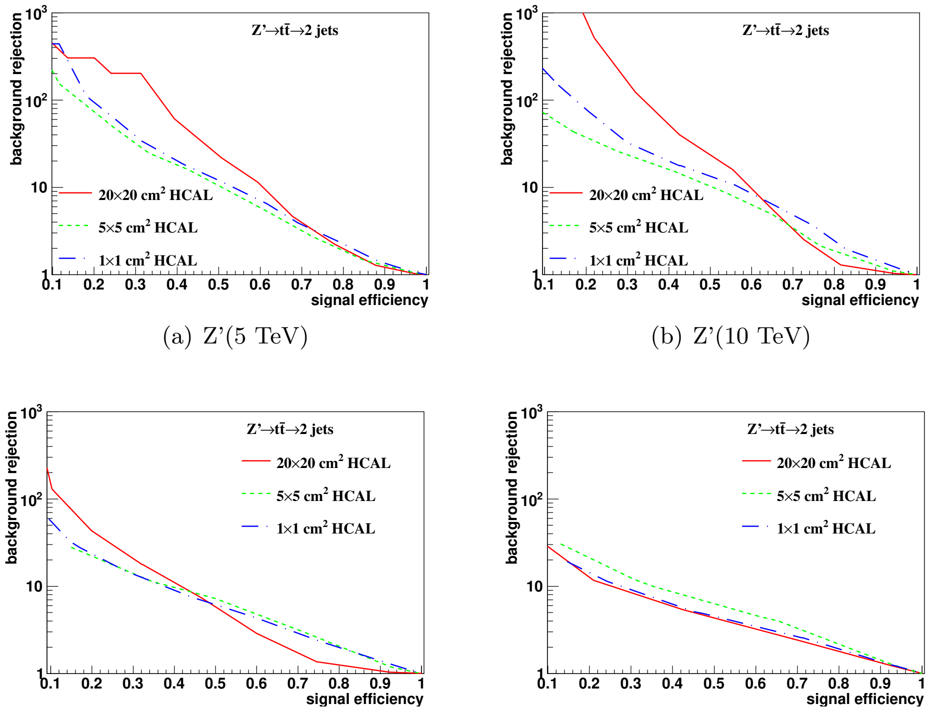

(a) Z'(5 TeV) (b) Z'(10 TeV)

(c) Z'(20 TeV) (d) Z'(40 TeV)

Figure 14: Signal efficiency versus background rejection rate using τ_{32}. Resonance masses of (a) 5 TeV, (b) 10 TeV, (c) 20 TeV and (d) 40 TeV are shown here. In each figure, the three ROC curves correspond to different HCAL cell sizes.

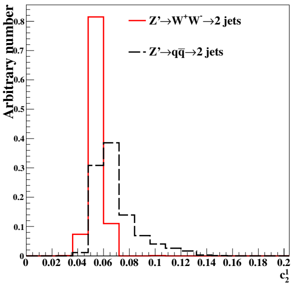

(a) 20×20 (cm^2)

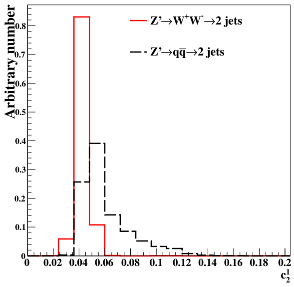

(b) 5×5 (cm^2)

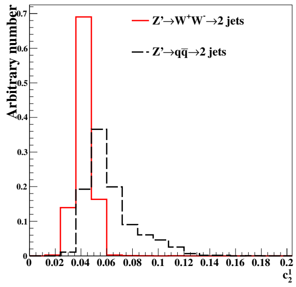

(c) 1×1 (cm^2)

Figure 15: Distributions of C_2^1 with $M(Z') = 20$ TeV for different detector granularities. Cell sizes of 20×20, 5×5, and 1×1 cm^2 are shown here.

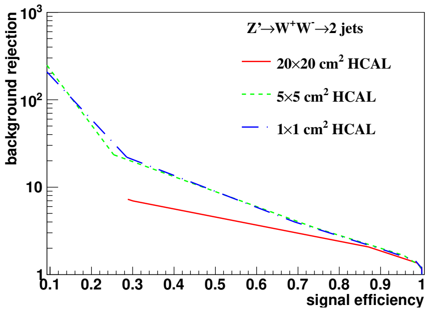

(a) Z'(5 TeV)

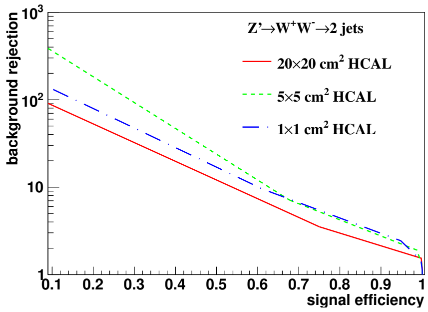

(b) Z'(10 TeV)

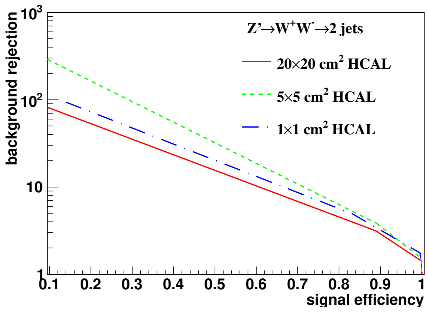

(c) Z'(20 TeV)

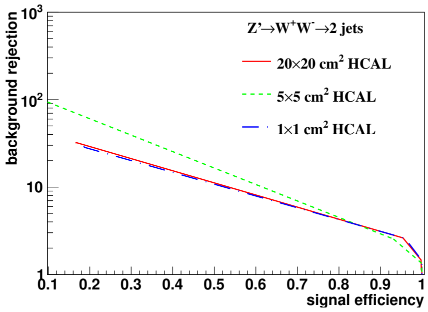

(d) Z'(40 TeV)

Figure 16: Signal efficiency versus background rejection rate using C_2^1. The resonance masses of (a) 5 TeV, (b) 10 TeV, (c) 20 TeV, and (d) 40 TeV are shown here. In each figure, the three ROC curves correspond to different detector sizes.

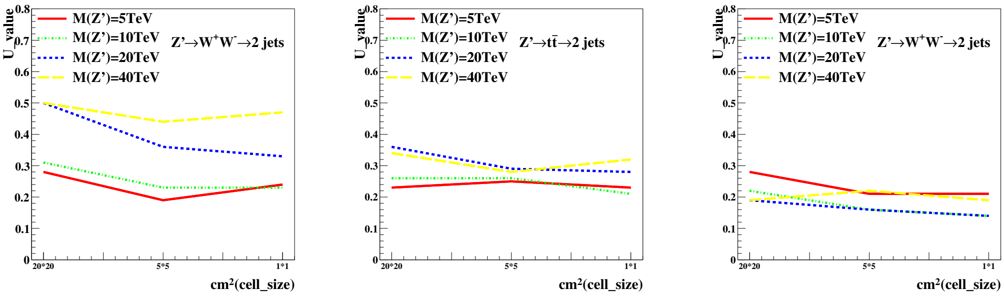

(a) τ_{21} (b) τ_{32} (c) $C_2^{(1)}$

Figure 17: The Mann-Whitney U values for τ_{21}, τ_{32}, and $C_2^{(1)}$ reconstructed for different resonance masses and detector cell sizes.

most cases, better than for a detector with 0.087×0.087 cells. The performance of the HCAL with cells $\Delta\eta \times \Delta\phi = 0.0087 \times 0.0087$ and $\Delta\eta \times \Delta\phi = 0.0043 \times 0.0043$ was found to be similar.

Thus this study confirms the HCAL geometry of the SiFCC detector [7], with the $\Delta\eta \times \Delta\phi = 0.022 \times 0.022$ HCAL cells. It also confirms the HCAL design of the baseline FCC-hh [19, 20] detector with $\Delta\eta \times \Delta\phi = 0.025 \times 0.025$ HCAL cells.

It interesting to note that, for very boosted jets with transverse momenta close to 20 TeV, no significant improvement with the decrease of cell sizes was observed. This result needs to be understood in terms of various types of simulations and different options for reconstruction of the calorimeter clusters.

Acknowledgements

This research was performed using resources provided by the Open Science Grid, which is supported by the National Science Foundation and the U.S. Department of Energy Office of Science. We gratefully acknowledge the computing resources provided on Blues, a high-performance computing cluster operated by the Laboratory Computing Resource Center at Argonne National Laboratory. Argonne National Laboratory is supported by the U.S. Department of Energy, Office of Science, Office of High Energy Physics under contract DE-AC02-06CH11357. The Fermi National Accelerator Laboratory (Fermilab) is operated by Fermi Research Alliance, LLC under Contract No. DE-AC02-07CH11359 with the United States Department of Energy.

References

[1] M. Benedikt, The Global Future Circular Colliders EffortCERN-ACC-SLIDES-2016-0016. Presented at P5 Workshop on the Future of High Energy Physics, BNL, USA, Dec. 15-18, 2013. URL http://cds.cern.ch/record/2206376

[2] J. Tang, et al., Concept for a Future Super Proton-Proton Collider (2015). arXiv:1507.03224.

[3] R. Calkins, et al., Reconstructing top quarks at the upgraded LHC and at future accelerators, in: Proceedings, Community Summer Study 2013: Snowmass on the Mississippi (CSS2013): Minneapolis, MN, USA, July 29-August 6, 2013. arXiv:1307.6908. URL https://inspirehep.net/record/1244676/files/arXiv:1307.6908.pdf

[4] S. V. Chekanov, J. Dull, Energy range of hadronic calorimeter towers and cells for high-pT jets at a 100 TeV collider.arXiv:1511.01468.

[5] E. Coleman, M. Freytsis, A. Hinzmann, M. Narain, J. Thaler, N. Tran, C. Vernieri, The importance of calorimetry for highly-boosted jet substructurearXiv:1709.08705.

[6] DELPHES 3 Collaboration, J. de Favereau, C. Delaere, P. Demin, A. Giammanco, V. Lematre, A. Mertens, M. Selvaggi, DELPHES 3, A modular framework for fast simulation of a generic collider experiment, JHEP 02 (2014) 057. arXiv:1307.6346, doi:10.1007/JHEP02(2014)057.

[7] S. V. Chekanov, M. Beydler, A. V. Kotwal, L. Gray, S. Sen, N. V. Tran, S. S. Yu, J. Zuzelski, Initial performance studies of a general-purpose detector for multi-TeV physics at a 100 TeV pp collider, JINST 12 (06) (2017) P06009. arXiv:1612.07291, doi:10.1088/1748-0221/12/06/P06009.

[8] J. Allison, et al., Recent developments in Geant4, Nuclear Instruments and Methods in Physics Research A 835 (2016) 186.

[9] M. J. Charles, PFA Performance for SiD, in: Linear colliders. Proceedings, International Linear Collider Workshop, LCWS08, and International Linear Collider Meeting, ILC08, Chicago, USA, Novermber 16-20, 2008 , 2009. arXiv:0901.4670.

[10] J. S. Marshall, M. A. Thomson, Pandora Particle Flow Algorithm, in: Proceedings, International Conference on Calorimetry for the High Energy Frontier (CHEF 2013), 2013, pp. 305–315. arXiv:1308.4537.

[11] G. P. S. M. Cacciari, G. Soyez, FastJet user manual CERN-PH-TH/2011-297. arXiv:1111.6097.

[12] M. Cacciari, G. P. Salam, G. Soyez, The anti-kt jet clustering algorithm, JHEP 0804 (2008) 063. arXiv:0802.1189.

[13] S. Chekanov, HepSim: a repository with predictions for high-energy physics experiments, Advances in High Energy Physics 2015 (2015) 136093, available as http://atlaswww.hep.anl.gov/hepsim/.

[14] B. Auerbach, S. Chekanov, J. Love, J. Proudfoot, A. Kotwal, Sensitivity to new high-mass states decaying to ttbar at a 100 TeV collider arXiv:1412.5951.

[15] J. Butterworth, B. Cox, J. R. Forshaw, WW scattering at the CERN LHC, Phys.Rev. D65 (2002) 096014. arXiv:hep-ph/0201098, doi:10.1103/PhysRevD.65.096014.

[16] S. Catani, Y. L. Dokshitzer, M. H. Seymour, B. R. Webber, Longitudinally-invariant k-clustering algorithms for hadron-hadron collisions, Nuclear Physics B 406 (12) (1993) 187 – 224. URL http://www.sciencedirect.com/science/article/pii/055032139390166M

[17] S. D. Ellis, D. E. Soper, Successive combination jet algorithm for hadron collisions, Phys. Rev. D48 (1993) 3160–3166. arXiv:hep-ph/9305266, doi:10.1103/PhysRevD.48.3160.

[18] ATLAS Collaboration Collaboration, G. Aad, et al., Jet mass and substructure of inclusive jets in $\sqrt{s} = 7$ TeV pp collisions with the ATLAS experiment, JHEP 1205 (2012) 128. arXiv:1203.4606, doi:10.1007/JHEP05(2012)128.

[19] C. Neubüser, Performance studies and requirements on the calorimeters for a fcc-hh experiment, in: Z.-A. Liu (Ed.), Proceedings of International Conference on Technology and Instrumentation in Particle Physics 2017, Springer Singapore, Singapore, 2018, pp. 37–43.

[20] J. Faltova, Design and performance studies of a hadronic calorimeter for a fcc-hh experiment, Journal of Instrumentation 13 (03) (2018) C03016. URL http://stacks.iop.org/1748-0221/13/i=03/a=C03016

[21] A. J. Larkoski, S. Marzani, G. Soyez, J. Thaler, Soft Drop, JHEP 05 (2014) 146. arXiv:1402.2657, doi:10.1007/JHEP05(2014)146.

[22] Y. L. Dokshitzer, G. D. Leder, S. Moretti, B. R. Webber, Better jet clustering algorithms, JHEP 08 (1997) 001. arXiv:hep-ph/9707323, doi:10.1088/1126-6708/1997/08/001.

[23] M. Wobisch, T. Wengler, Hadronization corrections to jet cross-sections in deep inelastic scattering,

in: Monte Carlo generators for HERA physics. Proceedings, Workshop, Hamburg, Germany, 1998-1999, 1998, pp. 270–279. arXiv:hep-ph/9907280.

[24] J. Thaler, K. Van Tilburg, Identifying Boosted Objects with N-subjettiness, JHEP 03 (2011) 015. arXiv:1011.2268, doi:10.1007/JHEP03(2011)015.

[25] S. Catani, Y. L. Dokshitzer, M. H. Seymour, B. R. Webber, Longitudinally-invariant $k_\perp$-clustering algorithms for hadron-hadron collisions, Nucl. Phys. B 406 (CERN-TH-6775-93. LU-TP-93-2) (1993) 187–224.

[26] F. A. Dreyer, L. Necib, G. Soyez, J. Thaler, Recursive Soft Drop, JHEP 06 (2018) 093. arXiv:1804.03657, doi:10.1007/JHEP06(2018)093.

[27] H. B. Mann, D. R. Whitney, On a test of whether one of two random variables is stochastically larger than the other, Ann. Math. Statist. 18 (1) (1947) 50–60. doi:10.1214/aoms/1177730491. URL https://doi.org/10.1214/aoms/1177730491

[28] A. J. Larkoski, G. P. Salam, J. Thaler, Energy Correlation Functions for Jet Substructure, JHEP 06 (2013) 108. arXiv:1305.0007, doi:10.1007/JHEP06(2013)108.